EES Catalysis

PAPER

View Article Online
View Journal | View Issue

Cite this: *EES Catal.*, 2025, 3, 1134

Inhibiting overoxidation of an α-MnO_2 electrocatalyst by the lattice strain effect for efficient water oxidation†

Fang-Yi Li,[a] Shan Guan,[b] Jianming Liu,[a] Changhao Liu,[a] Junfeng Zhang,[b] Ju Gu,[c] Zhaosheng Li,[a] Zhigang Zou[a] and Zhen-Tao Yu *[a]

Received 10th April 2025,
Accepted 4th June 2025

DOI: 10.1039/d5ey00106d

rsc.li/eescatalysis

The development of low-cost transition metal catalysts for use in alkaline water electrolysis (AWE) at high current densities is essential for achieving high-performance water splitting. Here, we reported a CrSb–MnO_2 catalyst, which shows a low overpotential of 263 mV at 100 mA cm^{-2} and outstanding stability with only a small degradation of the catalyst after 100 h of operation at 1 A cm^{-2} (1 M KOH). In addition, the catalyst also achieved excellent performance in AWE (1.69 V@1 A cm^{-2}). This enhanced performance is not only due to lattice-strain engineering, which effectively modulates the electronic configurations of the active sites, but also due to bimetallic synergy, which improves the dynamics of metal–metal charge transfer. *In situ* differential electrochemical mass spectrometry (DEMS) and Fourier-transform infrared (FTIR) analyses revealed that the CrSb–MnO_2 catalyst preferred the adsorbate evolution mechanism (AEM) during the alkaline OER. This preference contributes to sustained stability under high current conditions in alkaline media. This work offers a novel approach for designing membrane electrodes that can operate efficiently and stably under large currents.

Broader context

Electrochemical water splitting is an advanced technology for the large-scale production of renewable green hydrogen. However, the oxygen evolution reaction (OER) at the anode involves a slow four-electron transport process, which significantly restricts the overall oxygen evolution rate and the efficiency of water oxidation. The MnO_2 catalyst is widely utilized in alkaline electrolyzers due to its abundant valence states and low cost. Lattice strain engineering plays a crucial role in adjusting the electron configuration of metal sites and regulating the interaction between the catalytic surface and adsorbate molecules, which can effectively enhance the inherent activity of the MnO_2 catalyst. In this study, we report CrSb–MnO_2 nanosheets with lattice strain using a phonochemical method. Doping with high-valence atoms not only enhances the electrical conductivity of MnO_2 but also effectively balances the binding energy between the catalytic site and the oxygen intermediate. Additionally, it prevents the charge disproportionation reaction of Mn^{3+} at high currents, thereby improving the stability of the catalyst. The CrSb–MnO_2 catalyst shows excellent OER activity and stability at high temperatures and high current densities under alkaline conditions. This study provides valuable insights into the design of alkaline OER catalysts.

Introduction

Water electrolysis is generally considered to be one of the most promising technologies for the scalable production of green hydrogen. The oxygen evolution reaction (OER) at the anode is a four-electron process that is kinetically sluggish and significantly restricts the overall efficiency of electrochemical water splitting.[1] Among the electrolytic hydrogen production technologies, alkaline water electrolysis (AWE) employs low-cost transition metal-based catalysts, such as manganese (Mn), iron (Fe), cobalt (Co), and nickel (Ni), especially in the form of transition metal oxide catalysts, which are essential for large-scale commercial applications.[2–6] Energy efficiency in AWE decreases by at least 30% when operating at high temperatures (above 50 °C) and high current densities (over 0.3 A cm^{-2}). This reduction in efficiency occurs because the catalyst loses its activity and stability under these conditions. Therefore, it is essential to enhance the performance of electrocatalysts for their effective application in AWE.[7]

Manganese dioxide (MnO_2) has gained significant interest as an oxidation catalyst in alkaline water due to its high density

[a] National Laboratory of Solid State Microstructures and Jiangsu Provincial Key Laboratory for Nanotechnology, College of Engineering and Applied Sciences, Nanjing University, Nanjing, Jiangsu, 210093, China. E-mail: yuzt@nju.edu.cn
[b] State Key Laboratory of Engines, School of Mechanical Engineering, Tianjin University, Tianjin, 300350, China
[c] School of Physics, Nanjing University, Nanjing, 210093, People's Republic of China

† Electronic supplementary information (ESI) available. See DOI: https://doi.org/10.1039/d5ey00106d

of defect edges and its ability to exist in various valence states. Additionally, according to the OER volcano diagram for metal oxides, the MnO_2 catalyst exhibits activity comparable to that of noble metals.[8] α-MnO_2 features a large tunnelling structure that enhances the diffusion of reactant molecules, resulting in superior electrocatalytic activity compared to other crystalline forms of MnO_2.[9] Ma *et al.* reported that NiFe@α-MnO_2 nanosheets achieved an overpotential of 310 mV at a current density of 100 mA cm^{-2} in a 1 M KOH solution. The catalytic stability was maintained for approximately 100 hours at a current density of 0.2 A cm^{-2}.[10] Additionally, Kim *et al.* found that MnO_2 (Pruatronic®) electrocatalysts exhibited strong performance in alkaline water electrolysis (AWE), reaching 2.4 V at 1 A cm^{-2} with a loading of 2.5 mg cm^{-2} in a 1 M K_2CO_3 solution.[11] Although the performance is relatively outstanding, it has not reached the practical application requirements of AWE electrolytic cells (1.8 V@1 A cm^{-2}).[12] At high current densities (greater than 0.5 A cm^{-2}), Mn ions in MnO_2 are prone to overoxidation during operation. This process can lead to the formation of manganese tetraoxide (MnO_4^{2-}) or permanganate (MnO_4^{-}). Such overoxidation results in the loss of catalyst mass and a reduction in catalytic activity.[13] Furthermore, the inherent OER activity and low electrical conductivity of transition metal oxides limit their effectiveness as catalysts in water oxidation.

Lattice strain engineering improves catalyst activity and stability by introducing vacancy defects or by doping with various metal ions or non-metal components.[14] These modifications can alter metal coordination bonds through either stretching or compression. Recently, metal ions such as Mg, Fe, Co, Ni, Cu, Mo, and Ru have been identified as effective dopants for α-MnO_2 catalysts.[15,16] Recently, researchers have successfully developed IrO_2/α-MnO_2 and γ-MnO_2 catalysts that employ lattice strain-engineering. These catalysts show that interfacial lattice mismatch can enhance both the OER activity and stability in proton exchange membrane (PEM) systems.[17,18]

Doping transition metal oxides with high-valence metal ions improves their conductivity, which helps reduce energy loss in electrolyzers. The high-valence states of these metal ions enhance the electronic configuration of the e_g orbitals, effectively balancing the binding energy between catalytic sites and oxygen intermediates. As a result, this enhancement leads to improved catalytic performance.[19] For example, incorporating Cr atoms into MnFeCo alloys has been shown to enhance overall catalytic performance, resulting in a low overpotential of 295 mV at a current density of 100 mA cm^{-2}. According to d-band theory, the tensile strain introduced by adjacent Cr raises the d-band center of the active metal, which in turn affects the chemisorption of intermediates during the OER.[20] Nonetheless, the application of Cr-doped MnO_2 catalysts, utilizing lattice strain effects, to enhance catalyst performance in AWE remains limited. Additionally, achieving high stability in electrolyzers at elevated current densities presents a challenge due to the unavoidable phase separation between high-valent dopants and 3d metal sites. Bimetallic-doped catalysts demonstrate enhanced catalytic performance compared to those with a single metal ion. This improvement is largely attributed to the limited ability of single-doped catalysts to optimize OER activity. By altering the distribution of local electron density, bimetallic ions can enhance the synergistic and electronic effects among the different metals involved, thereby improving the stability and reaction rates of intermediates in catalytic processes.[21]

In this study, we synthesized α-MnO_2-based catalysts using a phonochemistry method followed by high-temperature calcination. The phonochemistry technique utilizes high-frequency ultrasound to induce cavitation bubbles, resulting in the formation of nanoscale particles with associated lattice defects (Fig. 1a).[22] We leveraged lattice strain to improve the performance of the α-MnO_2 catalyst in alkaline water oxidation. The CrSb–MnO_2 catalyst, with a Cr loading of about 2 wt% and an antimony (Sb) loading of about 1 wt%, demonstrated an overpotential of 263 mV at a current density of 100 mA cm^{-2} (240 mV@10 mA cm^{-2}) in a 1 M KOH solution, which is better than most of the reported MnO_2-based catalysts (>300 mV) (Fig. S1a, ESI†). Notably, this catalyst achieved an impressive performance of 1.69 V at 1 A cm^{-2} in alkaline water electrolysis and maintained stability at a large current of 1 A cm^{-2} for at least 100 h, outperforming most non-precious metal catalysts (Fig. S1b, ESI†). *In situ* measurements of DEMS and FTIR confirmed the role of the key reaction intermediate (*OOH) in the alkaline water oxidation process involving the CrSb–MnO_2 catalyst. Furthermore, it was demonstrated that the catalytic process follows the adsorbate evolution mechanism (AEM), which helps maintain stability under high current conditions in alkaline media.

Results and discussion

Morphology and structure

Introducing doping heteroatoms with different atomic radii can alter metal coordination bond lengths, change the M–O interaction, and modify the catalytic activity. Five metal atoms were chosen as dopants: Fe, Co, and Ni, which have smaller atomic radii than Mn, while Cr and Sb have larger atomic radii than Mn. We have prepared six catalysts using a phonochemical method, followed by annealing at 350 °C: FeNi–MnO_2, FeCo–MnO_2, CoNi–MnO_2, CrFe–MnO_2, CrCo–MnO_2, and CrSb–MnO_2. Among the catalysts tested, CrSb–MnO_2 demonstrated the highest efficiency for alkaline oxygen evolution in 1 M KOH, while CoNi–MnO_2 showed no performance improvement compared to α-MnO_2. Since lattice strain significantly influences catalyst activity, we chose CrSb–MnO_2 and CrCo–MnO_2 catalysts, which exhibit higher activity, to investigate the effects of bimetal-doping on the lattice strain effect through morphology and electronic structure analysis.

According to Bragg's rule, the lattice parameters of the host expand when subjected to high-temperature calcination or when doped with high-valence metal atoms or with metal dopants that have a larger atomic radius.[23,24] Fig. 2a shows that the XRD pattern of α-MnO_2 matches the standard phase, with no additional peaks detected, indicating the absence of impurity phase formation after doping. We observe that the

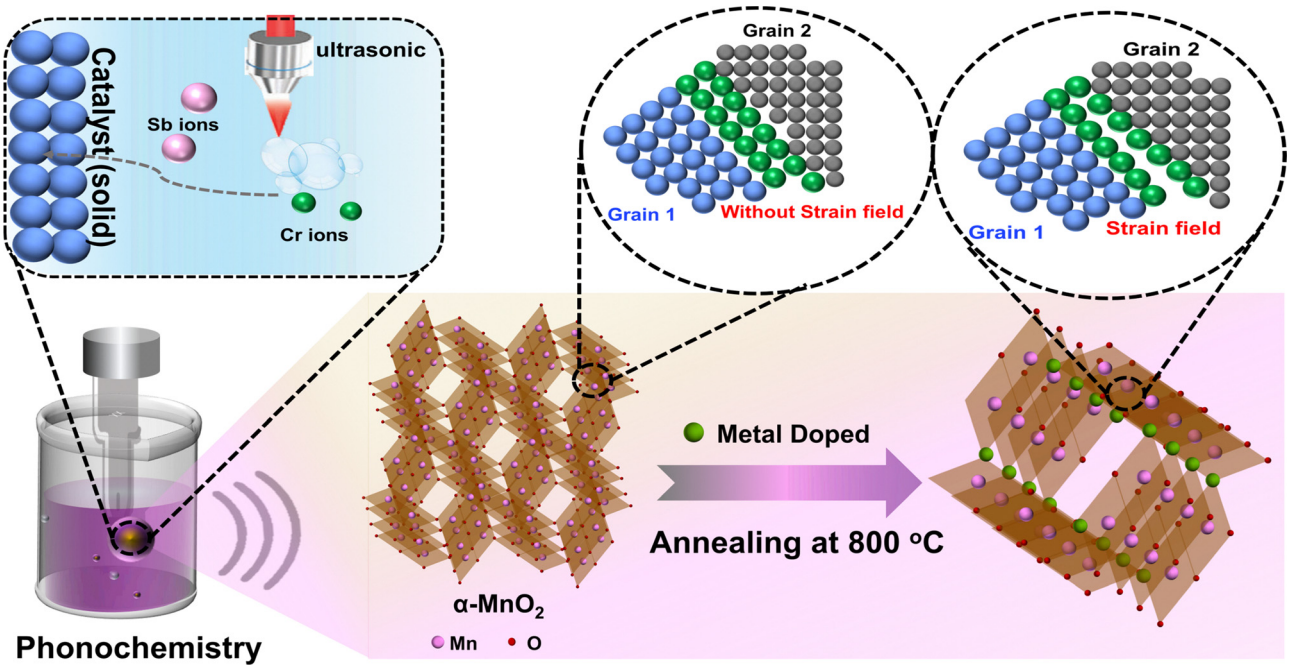

Fig. 1 Schematic for preparation of the bimetallic doped α-MnO_2 catalyst.

(211) planes shift towards a lower angle. This indicates an expansion of the lattice parameters of α-MnO_2 in the *c* direction.[23] When 2.2 wt% of Cr and 1.1 wt% of Sb are added to α-MnO_2 (ICP determined the content, Table S1, ESI†), the diffraction peak observed at 36.26° shifts to a lower angle by 0.15°. Similarly, with the inclusion of 2.5 wt% Cr and 1.3 wt% Co, this diffraction peak shifts slightly by 0.09° towards a lower angle. In contrast, when Fe, Co, and Ni are used as dopants, no significant shift in the diffraction peaks is observed. This indicates that introducing transition metals with larger atomic radii will efficiently generate tensile strain of the host MnO_2, because the doped M–O bond length can change the *ortho* Mn–O bond length.[25,26]

The atomic-resolution transmission electron microscopy (TEM) techniques enable precise measurement of the lattice

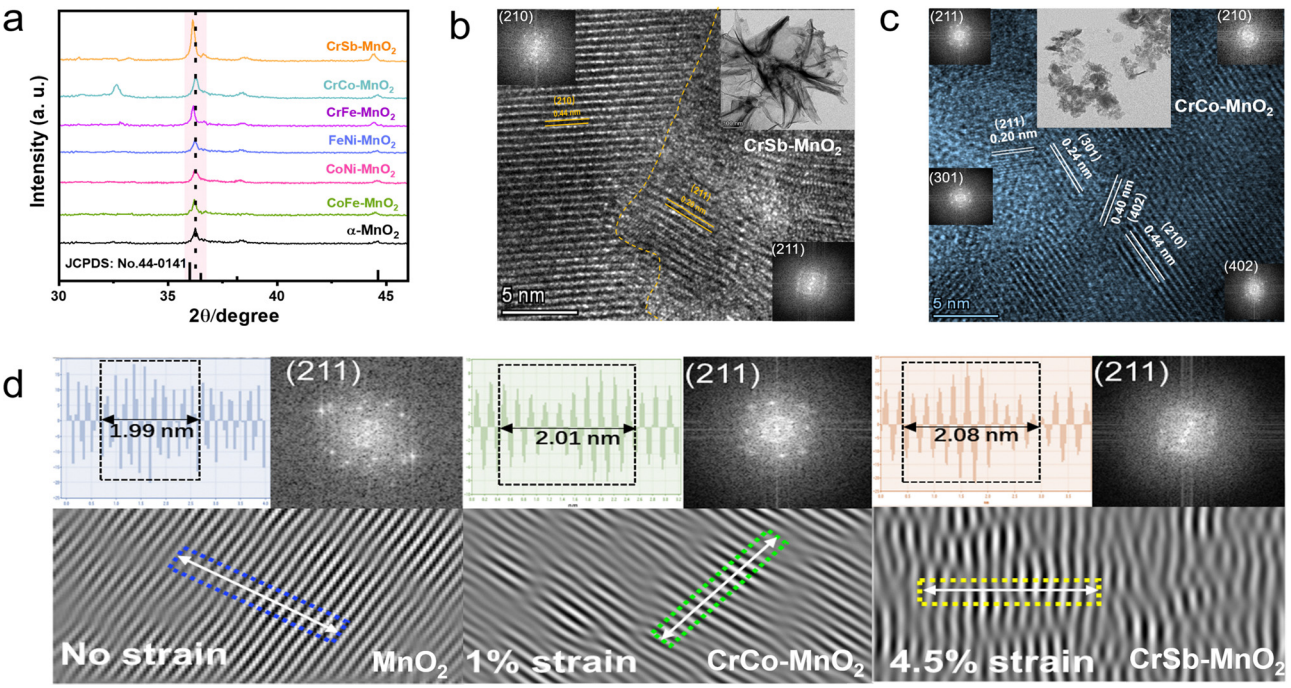

Fig. 2 (a) XRD patterns of bimetallic ion-doped α-MnO_2 and bare α-MnO_2. (b) and (c) TEM images of CrSb–MnO_2 and CrCo–MnO_2. (d) IFFT images of α-MnO_2, CrSb–MnO_2, and CrCo–MnO_2.

spacing of solid surfaces. As illustrated in Fig. 2b and c and Fig. S2 (ESI†), we obtained a clear distribution of the lattice fringes for the CrSb–MnO_2 and CrCo–MnO_2 catalysts, which allowed us to quantify the strain resulting from doping. We performed selected area electron diffraction (SAED) on specific regions of the TEM images, as illustrated in the insets of Fig. 2b and c. This analysis revealed that both CrSb–MnO_2 and CrCo–MnO_2 nanosheets exhibit a polycrystalline structure. Consistent with previous studies,[27] we focused on the most exposed (211) crystalline surface to analyze the lattice strain effects of the α-MnO_2 catalysts. The measured lattice spacings (*d*) for the (211) crystalline surfaces of the α-MnO_2, CrCo–MnO_2, and CrSb–MnO_2 catalysts were 1.99 Å, 2.01 Å, and 2.08 Å, respectively (Fig. 2d). The increase in the *d* value indicates that tensile strain forms after doping. This boosts the transition-metal d-band center and raises the antibonding d state, thereby strengthening the interaction between the active sites of the catalyst and reaction intermediate, which ultimately enhances electrocatalytic activity.[14] According to the equation in the literature (see ESI†),[28] we can evaluate the tensile strain intensity present within or on the surface of the catalyst. The incorporation of bimetallic ions modifies the metal coordination bonds, leading to tensile strains of 4.5% for the CrSb–MnO_2 catalyst and 1% for the CrCo–MnO_2 catalyst, respectively. This observation further supports that optimizing the surface geometry and electronic structure by adjusting the lattice spacing is possible. The XRD and TEM characterization clearly demonstrate the lattice strain effect in these samples, as the lattice distortion increases and the d-band center shifts away from the Fermi energy level.[29] Energy dispersive spectroscopy (EDS) analysis showed a diverse elemental composition and a uniform distribution of the CrSb–MnO_2 and CrCo–MnO_2 catalysts (Fig. S3 and Tables S2 and S3, ESI†). These findings are consistent with the results obtained from the ICP analysis.

The electronic structure and chemical valence states of elements in bimetallic-doped catalysts were analyzed using X-ray photoelectron spectroscopy (XPS) (Fig. 3a). In the Mn 2p spectrum, the area ratio of Mn^{3+} to Mn^{4+} in α-MnO_2 is approximately 0.35, indicating that defects contribute to the presence of Mn^{3+} in α-MnO_2.[30] The ratio of Mn^{3+} to Mn^{4+} in CrCo–MnO_2 is approximately 0.85, whereas in CrSb–MnO_2, this ratio is about 3.2. This indicates that the concentration of Mn^{3+} ions in CrSb–MnO_2 has increased, possibly due to a higher number of oxygen vacancies.[31] This result enhances the catalyst's adsorption capacity for intermediates in alkaline water oxidation.[32,33] Additionally, it has been observed that the Mn 2p spectrum of CrSb–MnO_2 and CrCo–MnO_2 is shifted to lower binding energies compared to that of α-MnO_2. This finding aligns with XPS results reported in the literature and can be attributed to the tensile strain introduced by the doping process with larger metal radius atoms.[34] The Cr 2p spectra of the Cr-doped catalysts reveal the presence of Cr^{6+} at 579.5 eV and Cr^{3+}–OH at 577.3 eV.[35] The peak area percentages for CrSb–MnO_2, are approximately 88.8% for Cr^{6+} and 11.2% for Cr^{3+}–OH, while the CrCo–MnO_2 catalyst shows relative peak area percentages of 55.6% for Cr^{6+} and 44.4% for Cr^{3+}–OH. This indicates that the CrSb–MnO_2 catalyst contains a higher proportion of high-valent Cr ions (Fig. 3b). Based on the previous

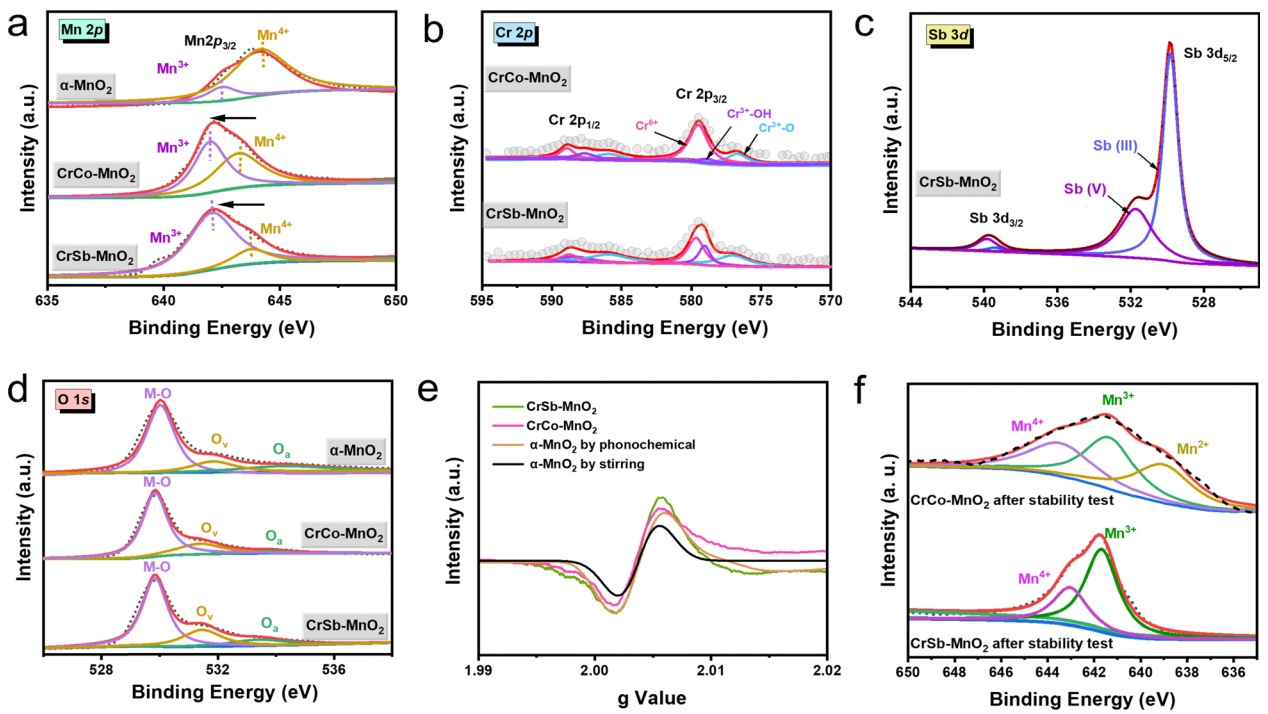

Fig. 3 XPS spectra of Mn 2p (a), O 1s (d) of CrSb–MnO_2, CrCo–MnO_2, and α-MnO_2, Cr 2p (b) of CrSb–MnO_2, CrCo–MnO_2, and Sb 3d (c) of CrSb–MnO_2. (e) EPR spectra of CrSb–MnO_2, CrCo–MnO_2, and α-MnO_2 at room temperature. (f) Mn 2p XPS spectrum of CrSb–MnO_2 and CrCo–MnO_2 catalysts after the activity experiment.

reports, non-3d high-valence transition-metal ions, particularly the 6+ metal ions, can effectively tailor electronic configurations and optimize adsorption energy values of 3d transition-metal-based electrocatalysts.[36,37] Additionally, Fig. 3d and Fig. S4 (ESI†) illustrate that the Sb ions in CrSb–MnO_2 exist as Sb(III) and Sb(IV), and Co ions in CrCo–MnO_2 are found in the trivalent oxidation state. Based on these results, the introduction of bimetallic atoms modifies the electronic structure of MnO_2, resulting in a distortion of its lattice structure. This distortion facilitates an increased flow of electrons from the bimetallic atoms to the Mn ions, which in turn raises the concentration of Mn^{3+} ions. A higher concentration of Mn^{3+} ions is essential for improving the performance of the OER.[38,39]

As illustrated in Fig. 3d, the high-resolution XPS spectrum of the O 1s region consists of three distinct components: 529.8 eV for lattice oxygen (M–O), 531.5 eV for oxygen vacancies (O_v), and 533.4 eV for surface-adsorbed oxygen (O_a).[40] The peak area percentages for M–O bonds, O_v, and O_a in CrCo–MnO_2 are 82.3%, 4.4%, and 7.3%, respectively. In contrast, the proportions of M–O and O_v in CrSb–MnO_2 increased to 84.6% and 13.0%, respectively, and that of the O_a decreased to 2.4%. The content of O_v in the CrSb–MnO_2 and CrCo–MnO_2 catalysts was significantly higher than that in the α-MnO_2 catalysts. This aligns with studies in the literature showing that high-valence metal ions can increase the concentration of oxygen vacancies.[41] The oxygen vacancies in metal oxides play a crucial role in optimizing the electronic structure of the metal surface and enhancing the intrinsic activity of the reactive sites.[42] Electron paramagnetic resonance (EPR) studies further confirmed the presence of oxygen vacancies (O_v) in the catalysts (Fig. 3e). The results indicate that MnO_2 synthesized using the phonochemical method produced a higher number of O_v compared to MnO_2 prepared using the stirring method. This difference can be attributed to the addition of Tween 85 with the ultrasound effect.[43]

Electrocatalytic performance

The electrocatalytic activity of bimetallic-doped MnO_2 catalysts was evaluated in an alkaline electrolyte (1 M KOH) using linear scanning voltammetry (LSV) in a three-electrode system. As illustrated in Fig. 4a and Fig. S5 (ESI†), the CrSb–MnO_2 catalyst demonstrated the best oxygen evolution performance, compared with Cr–MnO_2, FeNi–MnO_2, CoFe–MnO_2, and CoNi–MnO_2. It only requires an overpotential of 263 mV to achieve a current density of 100 mA cm^{-2}. Such an overpotential is significantly lower than that of currently published MnO_2 and other Mn-based catalysts.[44–47] The overpotential for CrSb–MnO_2 was approximately 240 mV at a current density of 10 mA cm^{-2} (Fig. S6, ESI†). The NiCo–MnO_2 catalyst showed the lowest catalytic activity of those bimetallic dopants, which requires approximately 1.66 V (*vs.* RHE) to achieve a current density of 100 mA cm^{-2}. The cyclic voltammetry (CV) results for the α-MnO_2-based catalyst in a 1 M KOH aqueous solution, using a glassy carbon electrode, revealed a redox couple associated with the transition of Mn^{3+} to Mn^{4+} at 1.28 V for the CrSb–MnO_2

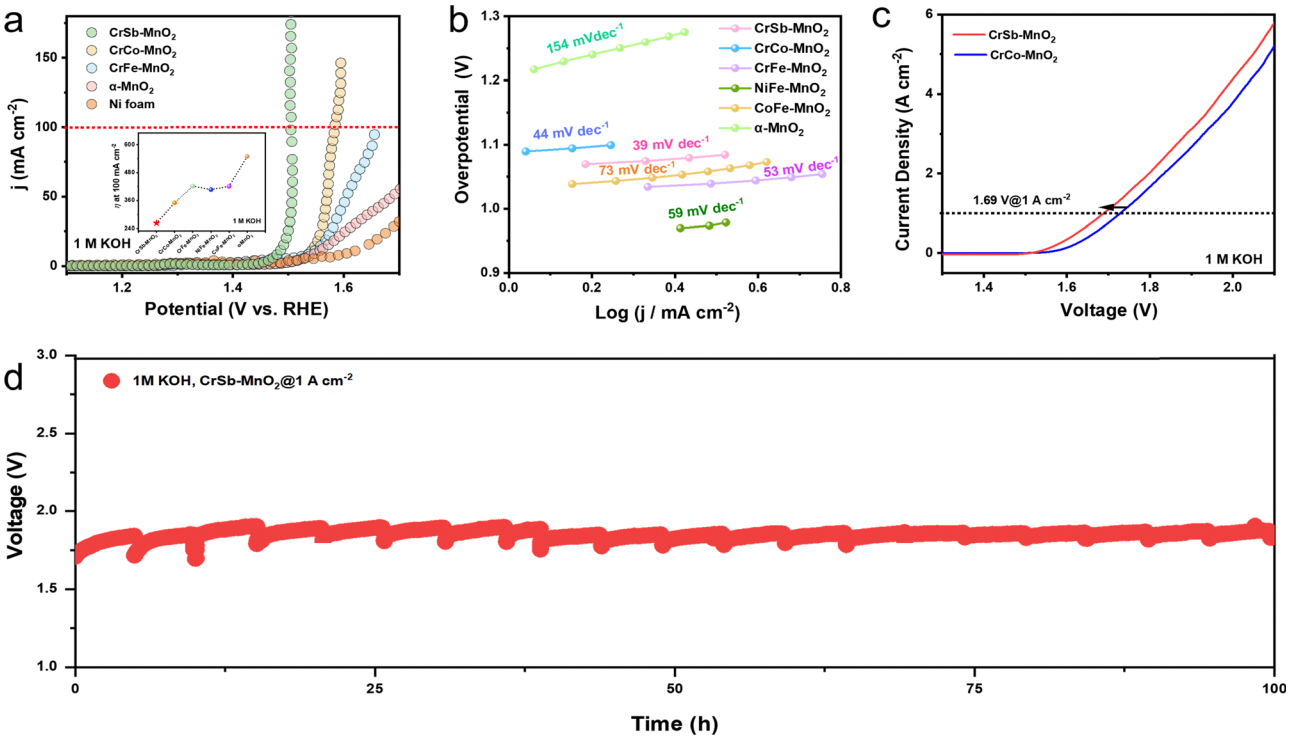

Fig. 4 (a) LSV polarization curves of CrSb–MnO_2, CrCo–MnO_2, CrFe–MnO_2, α-MnO_2, and Ni foam in 1 M KOH electrolyte at 100 mA cm^{-2} (the inset picture is a comparison of η of all the synthesized catalysts at 100 mA cm^{-2}). (b) Tafel slope plot of CrSb–MnO_2, CrCo–MnO_2, CrFe–MnO_2, NiFe–MnO_2, CoFe–MnO_2, and α-MnO_2. (c) The AWE polarization curves of CrSb–MnO_2 and CrCo–MnO_2 as anodes at 60 °C in 1 M KOH. (d) Stability of CrSb–MnO_2 by the chronopotentiometry technique at the constant current densities of 1 A cm^{-2}.

catalyst (Fig. S7, ESI†). CrSb–MnO_2 showed the lowest Tafel slope at 39 mV dec^{-1} among the tested materials, which is also lower than those for most reported transition metal alkaline catalysts (Fig. 4b).[48–52] Furthermore, CrSb–MnO_2 displayed the lowest charge transfer resistance in the electrochemical impedance spectroscopy (EIS) experiment, indicating its improved conductivity and quicker charge transfer rate, compared with other bimetallic doped MnO_2 catalysts (Fig. S8a, ESI†). These results suggested that valence electrons from doped heteroatoms enhance the hybridization between atoms and reduce resistance.[53]

Electrocatalytic performance

To evaluate the intrinsic OER activity of the CrSb–MnO_2 catalyst, we measured the electrochemical double-layer capacitance (C_{dl}) to determine the electrochemically active surface area (ECSA) (Fig. S8b and Fig. S9, ESI†). The ECSA of CrSb–MnO_2 was found to be 167.42 cm^2, approximately 5.43 times greater than that of α-MnO_2 (30.86 cm^2). This significant increase in ECSA indicates more active sites available in CrSb–MnO_2. Fig. S10 (ESI†) indicates that in a three-electrode system, CrSb–MnO_2 maintains its OER activity for at least 60 h at a current density of 10 mA cm^{-2}. In contrast, α-MnO_2 can only sustain its performance for approximately 13 h under the same current density in the three-electrode system.

The electrochemical structure and composition of the CrSb–MnO_2 and CrCo–MnO_2 catalysts were analyzed using XPS after completing a stability test (Fig. 4f). In the case of CrCo–MnO_2, the proportion of Mn^{3+} decreased from 56% to 31% before and after water oxidation. Meanwhile, the proportions of Mn^{4+} and Mn^{2+} increased by 7% and 32%, respectively. In contrast, CrSb–MnO_2 exhibited a decline in Mn^{3+} from 83% to 75%, while the proportion of Mn^{4+} increased by 8%, and no Mn^{2+} was detected. Besides, Cr^{3+} in the CrSb–MnO_2 catalyst after the stability experiment was readily oxidized to Cr^{6+} during the OER process (Fig. S11, ESI†).[54] The oxidation process played a crucial role in regulating the valence state of the active metal sites, which in turn facilitated the adsorption and desorption of intermediates involved in the OER. In MnO_2-based catalysts, the breaking of the Mn–O bond aids in dissolving Mn^{3+}, leading to the formation of either Mn^{2+} or Mn^{4+}, which contributes to structural collapse during water oxidation.[55] The results indicated that the doping of Cr inhibited the peroxidation of Mn^{3+}, a key factor in the water oxidation process.

To further evaluate the performance of the MnO_2-based catalyst in an industrial operating system, the CrSb–MnO_2 catalysts were tested in the AME water electrolyzer device. Each point on the polarization curves was obtained from measurements taken at constant voltage. As illustrated in Fig. 4c, the CrSb–MnO_2 cell achieved a current density of 1.0 A cm^{-2} at an applied voltage of 1.69 V (1.99 V@4.43 A cm^{-2}), surpassing the CrCo–MnO_2 cell, which had a voltage of 1.73 V under the same current density (1.99 V@3.69 A cm^{-2}). The enhancement was especially larger in the high current density region. The CrSb–MnO_2 anode shows improved performance compared to recently reported transition metal-based electrodes (Fe, Co, and Ni) such as Fe_xNi_yOOH, NiFeAl and $CoCrO_x$ and is comparable to noble-metal-based anion exchange membranes such as IrO_2/Ni foam (Table S4, ESI†). The ohmic resistance in the AWE electrolyzer was reduced in the CrSb–MnO_2 catalyst compared to CrCo–MnO_2 catalysts, indicating that the enhanced electrical conductivity of the CrSb–MnO_2 catalyst improved the PEM water electrolyzer performance (Fig. S12, ESI†).[56] The long-term stability performance of CrSb–MnO_2 was assessed, as the stability of the catalyst is vital for its practical applications. The stability tests for CrSb–MnO_2 and CrCo–MnO_2 catalysts, using the constant voltage method, were conducted under harsh industrial conditions. The CrSb–MnO_2 cell exhibited remarkable stability during continuous operation for 100 h at a current density of 1 A cm^{-2}, showing no significant degradation or reduction in activity (Fig. 4d and Table S4, ESI†). In contrast, the CrCo–MnO_2 cell experienced a notable decrease in performance after just 60 h of continuous operation (Fig. S13, ESI†). The ICP-MS results of the electrolyte after a stability test in 1 M KOH indicated that the dissolution of Mn ions in the CrSb–MnO_2 catalyst was lower than that observed in previously reported Mn-based catalysts (Tables S5 and S6, ESI†). These results demonstrate a substantial increase in the activity and stability of the CrSb–MnO_2 electrodes under harsh industrial conditions, making them suitable for AWE applications.

Oxygen evolution mechanism

During the water oxidation process, Mn^{3+} ions are formed through electron injection from water. Due to charge disproportionation, these Mn^{3+} ions can be converted into either Mn^{2+} or Mn^{4+}. To ensure the stability of the catalytic process, Mn^{2+} must be electrochemically reoxidized back to Mn^{3+}, which occurs at approximately 1.4 V.[57] This reoxidation is a crucial step in determining the oxygen evolution rate during the OER and is essential for maintaining catalytic stability. In alkaline electrolytes, the formation of Mn^{3+} is encouraged, which enhances its catalytic activity.[58] However, the degeneration of the e_g orbital in Mn^{3+} leads to an imbalance in its charge ratio, resulting in instability. Introducing vacancies or external metals is an effective approach to adjust the bond length and valence state of Mn, ultimately stabilizing the charge ratio of Mn^{3+}.[59] To investigate changes in the valence state of Mn during the alkaline OER of α-MnO_2 and CrSb–MnO_2 catalysts, we conducted *in situ* spectroelectrochemistry experiments from 0 V to 1.8 V (*vs.* RHE). As shown in Fig. 5a and b, when the electrode potential was set at 1.1 V (*vs.* RHE), a new absorption peak appeared at approximately 520.1 nm in the α-MnO_2 catalyst.[60] The intensity of this peak gradually increased as the voltage rose from 1.1 V to 1.7 V (*vs.* RHE). This new absorption band closely matches those reported in the literature and is attributed to the d–d transition of Mn^{3+} ions formed on the surface of anodically oxidized MnO_2 electrodes. The results show that the ratio of Mn^{3+} increases with the increase of voltage. We observed a red shift in the absorption peak of Mn^{3+} in the CrSb–MnO_2 catalyst. This shift indicates that the incorporation of Cr atoms, which have a larger atomic radius, leads to lattice distortion and an increase in the bond length of

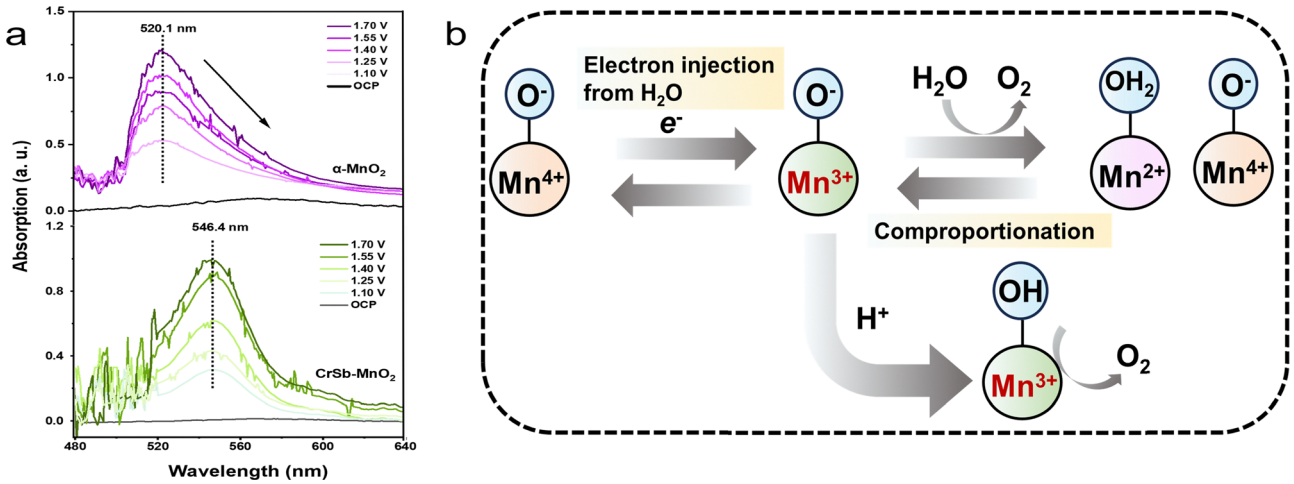

Fig. 5 (a) Absorption spectrum of the intermediate species on α-MnO_2 and CrSb–MnO_2 catalysts, from 1.1 to 1.7 V *vs.* RHE. (b) Oxidation states of Mn ions involved in the electro-oxidation of water to oxygen on a CrSb–MnO_2 catalyst in alkaline electrolyte.

Mn–O bonds.[61] This lattice distortion plays a crucial role in regulating the valence state of the active metal site of MnO_2.[62]

MnO_2-based catalysts facilitate water oxidation primarily through two mechanisms: the adsorbate evolution mechanism (AEM) and the lattice oxygen oxidation mechanism (LOM) (Fig. S14, ESI†). Research has shown that the AEM pathway, which involves the *OOH intermediate, is more effective than the LOM pathway that includes the *O–*O intermediate, in enhancing the stability of MnO_2 catalysts. The *O–*O intermediates can create vacancies in the lattice structure, which may ultimately lead to the collapse and dissolution of the catalyst, posing challenges for its stability.[63] The AEM mechanism is preferred for the oxygen evolution process on the (211) crystal surface, as it helps maintain the stability of the crystal structure, even under elevated anode potentials.[64]

In situ FTIR spectroscopy was used to investigate the mechanism of the OER and to identify the intermediates formed during the electrocatalytic process. These tests were conducted at various potentials, ranging from the open-circuit potential (OCP) up to 1.6 V (*vs.* RHE). In Fig. 6a, for the CrSb–MnO_2 system, as the applied potential increases, the driving force on the electrode surface also increases. This enhances the

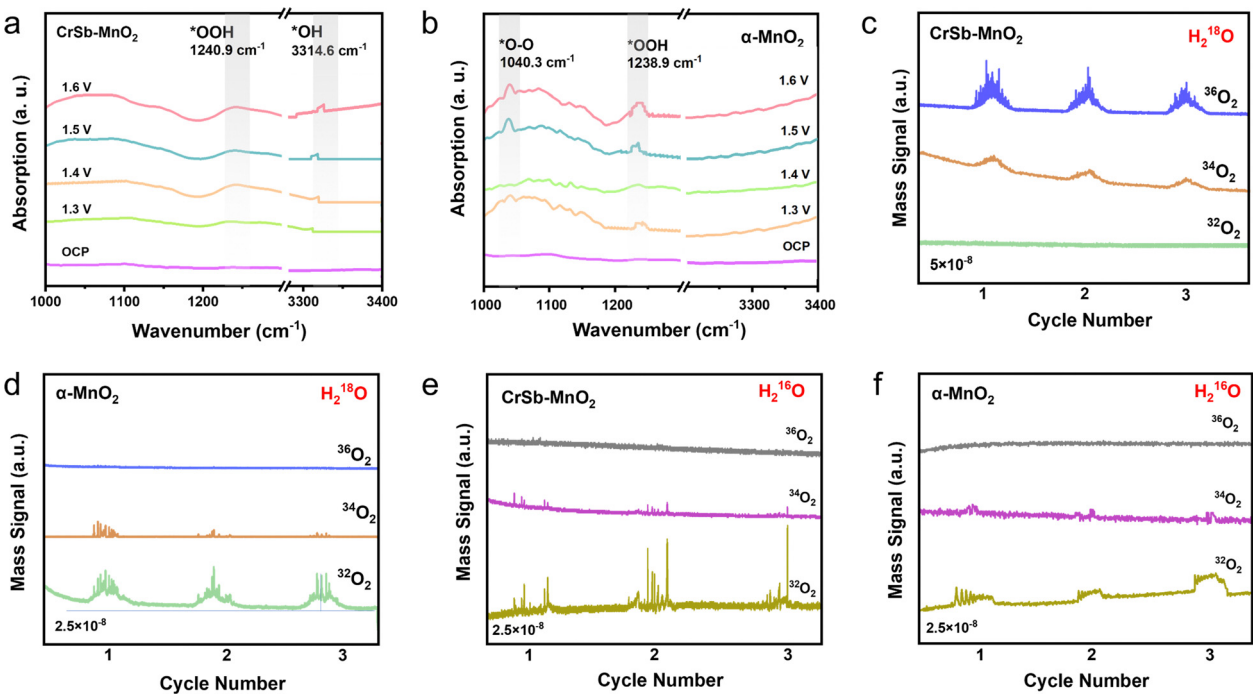

Fig. 6 (a) and (b) *In situ* FTIR spectra of CrSb–MnO_2 and α-MnO_2, respectively. (c) and (d) DEMS signals of O_2 products for CrSb–MnO_2 and α-MnO_2 using $H_2{}^{18}O$ and (e) and (f) $H_2{}^{16}O$ as the reaction medium, respectively.

generation rate of the intermediates *OH and *OOH, leading to a higher concentration of these intermediates. Consequently, a distinct absorption peak is observed at approximately 1240.9 cm^{-1}. The O–H vibration peak appeared at 3314.6 cm^{-1}, which was attributed to the characteristic vibrational adsorption of the *OOH intermediate.[65] As shown in Fig. 6b for α-MnO_2, a peak for the *OOH intermediate is observed at approximately 1240.9 cm^{-1}. Additionally, a signal peak corresponds to the *O–*O intermediate, which appears around 1056 cm^{-1}. The production of *O–*O intermediates is associated with the lattice oxygen oxidation mechanism (LOM), and this peak becomes more pronounced as the potential increases.[61] These indicate that the AEM and the LOM are involved in the OER process of α-MnO_2. It has been demonstrated that the release of lattice oxygen through the LOM mechanism accelerates the dissolution and overoxidation of α-MnO_2.[18] The instability of α-MnO_2 catalysts was linked to lattice oxygen involvement. Thus, CrSb–MnO_2 was primarily characterized by AEM during the OER process, demonstrating its effectiveness in suppressing the LOM pathway.

Using ^{18}O isotope-labeled differential electrochemical mass spectrometry (DEMS), we further verify the OER process of CrSb–MnO_2 preferred AEM, which restrains the overoxidation and dissolution of Mn species. As shown in Fig. 6a and b, mass signals corresponding to $^{34}O_2$ (^{16}O–^{18}O) and $^{36}O_2$ (^{18}O–^{18}O) were detected for the CrSb–MnO_2 catalysts during the OER process. The signal for $^{36}O_2$ originates from the $^{18}O_2$ in the electrolyte, while the $^{34}O_2$ signal arises from the lattice oxygen in the oxide catalyst that has not been isotopically substituted.[59,66] For the α-MnO_2 catalyst the mass signals for $^{32}O_2$ and $^{34}O_2$ were detected. The signal of $^{32}O_2$ (^{16}O–^{16}O) indicates that ^{16}O in the lattice is directly involved in the production of O_2, and if the lattice oxygen combines with ^{18}O in the electrolyte then the signal of $^{34}O_2$ is produced.[59,67]

We also performed a quantitative analysis to compare the percentage of oxygen originating from the lattice *versus* that from the electrolyte. The results showed that the proportion of lattice oxygen in CrSb–MnO_2 (16.2%) was significantly lower than that in α-MnO_2 (64.8%). This indicates that CrSb–MnO_2 favors oxygen evolution through the AEM rather than the LOM, as illustrated in Table S7 (ESI†).[68,69] After cleaning the catalyst surface using $H_2{}^{16}O$, we placed electrodes with the α-MnO_2 and CrSb–MnO_2 catalysts into the $H_2{}^{16}O$ electrolyte. During the oxygen evolution process, we detected a strong signal for $^{32}O_2$ and a very weak signal for $^{34}O_2$ (^{16}O–^{18}O) from both the α-MnO_2 and CrSb–MnO_2 catalysts. Notably, there was no signal for $^{36}O_2$ (^{18}O–^{18}O) observed (Fig. 6e and f). Following quantitative calculations, we found that the ratio of $^{34}O_2$ (^{16}O–^{18}O) to $^{32}O_2$ (^{16}O–^{16}O) in CrSb–MnO_2 (21%) is significantly lower than that in α-MnO_2 (37%). This preference contributes to the enhanced stability of the oxygen evolution at high current densities.

The theoretical calculations suggest that CrSb–MnO_2 is the optimal configuration for AEM when compared to Cr–MnO_2 and α-MnO_2. This configuration effectively lowers the energy barrier for the adsorption of *O and facilitates the rapid formation of *OOH in AEM. The improvement is attributed to the combined effects of electronic interactions and tensile strain present in the bimetallic doped Mn-based catalysts. These factors reduce the binding energy of *O and *OOH at the active sites, resulting in faster reaction kinetics.[70–72] At a voltage of $U = 0$ V, all reaction steps are endothermic processes (Fig. S15, ESI†). In contrast, the step from *O to *OOH at $U = 1.23$ V (Fig. 7b) is identified as the potential-determining step (PDS) for the OER. This step is characterized by having the maximum energy difference (ΔG) among all intermediate conversions that occur during the alkaline OER.[70,73] Notably, the *O formation step on $CrSbO_2$ exhibits the lowest energy barrier at −0.12 eV when compared to Cr–MnO_2 and α-MnO_2.

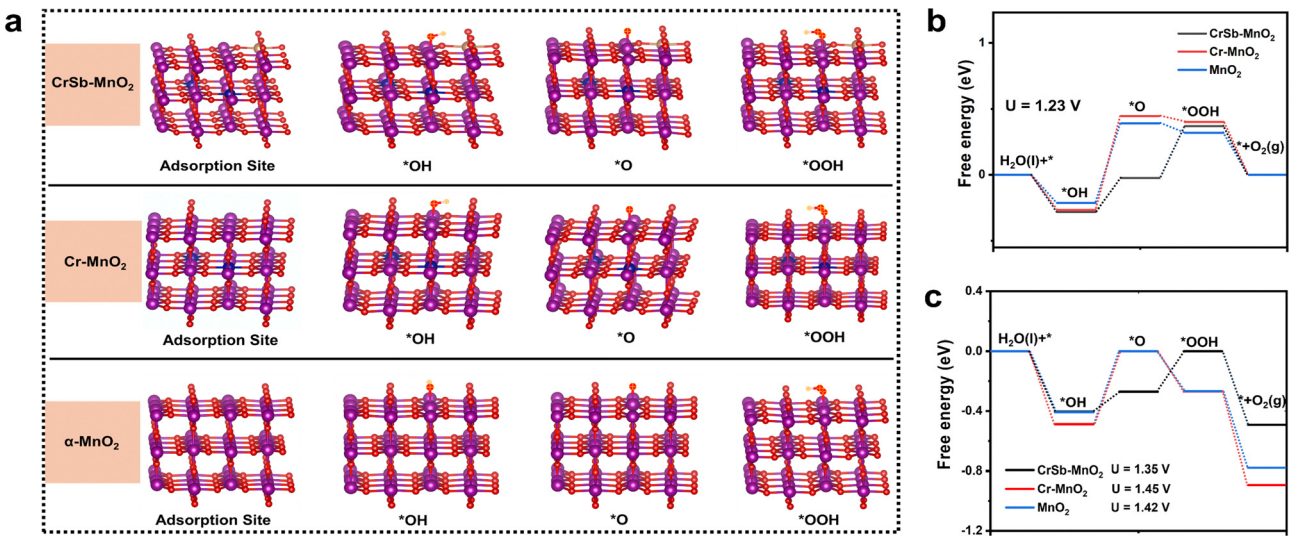

Fig. 7 (a) Structural models of the adsorption configurations of reaction intermediates (adsorption site, *OH, *OOH) of CrSb–MnO_2, Cr–MnO_2, and α-MnO_2 (purple ball: Mn atom; red ball: O atom; bule ball: Cr atom; brown ball: Sb atom). (b) The energy profile of the OER at $U = 1.23$ V. (c) The computed average adsorption energies for CrSb–MnO_2, Cr–MnO_2, and α-MnO_2.

This suggests that the process is advantageous for the rapid formation of *OOH.[70] As illustrated in Fig. 7c, CrSb–MnO_2 shows the lowest free energy barrier compared to Cr–MnO_2 and α-MnO_2, indicating that it requires the least potential to drive the OER. These findings highlight that incorporating Cr and Sb into the MnO_2 lattice significantly enhances OER activity.[74]

Conclusions

In this study, a CrSb–MnO_2 catalyst was synthesized through a combination of phonochemistry and high-temperature calcination. This catalyst demonstrated significantly enhanced OER durability and exhibited low overpotentials in alkaline electrolytes. The CrSb–MnO_2 electrode demonstrated a current density of 1.0 A cm^{-2} at 1.69 V and sustained this current density for over 100 hours. The improved activity and stability of the CrSb–MnO_2 catalyst in the OER can be attributed to the bimetal doping, which creates a lattice strain effect. This tensile effect effectively adjusts the electronic structure of the metal surface, enhancing the intrinsic activity of the bimetallic catalyst while preventing the overoxidation and dissolution of Mn species. *In situ* FTIR and DEMS analyses indicate that the CrSb–MnO_2 catalyst prefers the AEM mechanism over the LOM mechanism during the OER process, contributing to its stability under high current conditions in alkaline media. This study presents a method for non-precious metal catalysts to maintain high activity and stability in high-current practical industrial applications.

Author contributions

F. Y. L.: performing the experiments, collecting and analyzing the data, and writing the manuscript; G. S.: performing the AWE measurements; L. J. M. and L. C. H.: performing *in situ* FTIR spectroscopy and DEMS measurements; Z. T. Y., Z. G. Z., Z. S. L., and J. G.: resources, supervision, and editing. All authors read and commented on the manuscript.

Data availability

All relevant data are within the manuscript and its ESI.†

Conflicts of interest

There are no conflicts of interest to declare.

Acknowledgements

This work was financially supported by the National Key R&D Program of China (Grant No. 2021YFF0500502 and the National Science Foundation of China (Grant No. 22379064).

References

1 Y. Liu, D. Zhou, T. Deng, G. He, A. Chen, X. Sun, Y. Yang and P. Miao, *ChemSusChem*, 2021, **14**(24), 5359–5383.
2 A. A. Feidenhans'l, Y. N. Regmi, C. Wei, D. Xia, J. Kibsgaard and L. A. King, *Chem. Rev.*, 2024, **124**(9), 5617–5667.
3 H. Wang, T. Zhai, Y. Wu, T. Zhou, B. Zhou, C. Shang and Z. Guo, *Adv. Sci.*, 2023, **10**(22), 2301706.
4 S. Cherevko, S. Geiger, O. Kasian, N. Kulyk, J.-P. Grote, A. Savan, B. R. Shrestha, S. Merzlikin, B. Breitbach, A. Ludwig and K. J. J. Mayrhofer, *Catal. Today*, 2016, **262**, 170–180.
5 L. Bai, X. Wen and J. Guan, *ACS Appl. Energy Mater.*, 2019, **2**(8), 5584–5590.
6 A. A. Lourenço, V. D. Silva, R. B. da Silva, U. C. Silva, C. Chesman, C. Salvador, T. A. Simões, D. A. Macedo and F. F. da Silva, *J. Colloid Interface Sci.*, 2021, **582**, 124–136.
7 Y. Chen, Q. Li, Y. Lin, J. Liu, J. Pan, J. Hu and X. Xu, *Nat. Commun.*, 2024, **15**, 7278.
8 I. C. Man, H.-Y. Su, F. Calle-Vallejo, H. A. Hansen, J. I. Martínez, N. G. Inoglu, J. Kitchin, T. F. Jaramillo, J. K. Nørskov and J. Rossmeisl, *ChemCatChem*, 2011, **3**(7), 1159–1165.
9 Y. Meng, W. Song, H. Huang, Z. Ren, S.-Y. Chen and S. L. Suib, *J. Am. Chem. Soc.*, 2014, **136**(32), 11452–11464.
10 Y. Ma, M.-X. Li, H.-Y. Wang, Y. Wang, Y.-M. Chai and B. Dong, *Catal. Commun.*, 2022, **162**, 106380.
11 C. Kim, C. Dunn, M. J. Salgado, K. J. Beiler, J. L. Hawks, I. Wu, M.-C. Kuo and A. M. Herring, *J. Electrochem. Soc.*, 2024, **171**, 034502.
12 Q. Zhang, Y. Shan, J. Pan, P. Kumar, M. J. Keevers, J. Lasich, G. Kour, R. Daiyan, I. Perez-Wurf, L. Thomsen, S. Cheong, J. Jiang, K.-H. Wu, C.-L. Chiang and K. Grayson, *Sci. Adv.*, 2025, **11**, eads0836.
13 X. Zhang, M. Jin, F. Jia, J. Huang, A. Amini, S. Song, H. Yi and C. Cheng, *Energy Environ. Mater.*, 2023, **6**(5), e12457.
14 Z. Hou, C. Cui, Y. Li, Y. Gao, D. Zhu, Y. Gu, D. Zhu, Y. Gu, G. Pan, Y. Zhu and T. Zhang, *Adv. Mater.*, 2023, **35**(39), 2209876.
15 D. J. Davis, T. N. Lambert, J. A. Vigil, M. A. Rodriguez, M. T. Brumbach, E. N. Cokerer and S. J. Limmer, *J. Phys. Chem. C*, 2014, **118**(31), 17342–17350.
16 J. Jia, L. Li, X. Lian, M. Wu, F. Zheng, L. Song, G. Hu and H. Niu, *Nanoscale*, 2021, **13**(25), 11120–11127.
17 W. Sun, Z. Zhou, W. Q. Zaman, L. Cao and J. Yan, *ACS Appl. Mater. Interfaces*, 2017, **9**(48), 41855–41862.
18 Y. Song, J. Qian, S. Li, Z. Zhao, H. Cheng, K. Zou, Z. Han, Z. Li, H. Li, H. Zhou and M. Shao, *Angew. Chem., Int. Ed.*, 2025, e202502847.
19 H. Wang, T. Zhai, Y. Wu, T. Zhou, B. Zhou, C. Shang and Z. Guo, *Adv. Sci.*, 2023, **10**(22), 2301706.
20 T. Xiao, C. Sun and R. Wang, *J. Mater. Sci. Technol.*, 2024, **200**, 176–184.
21 J. Jiang, X.-L. Zhou, H.-G. Lv, H.-Q. Yu and Y. Yu, *Adv. Funct. Mater.*, 2023, **33**(10), 2212160.
22 T. Li, S. Deng, H. Liu and J. Chen, *Chem. Rev.*, 2024, **124**(11), 7045–7105.

23 Y. Song, J. Yang and X.-Q. Gong, *Top. Catal.*, 2015, **58**, 675–681.
24 W. Sun, Z. Wang, W. Q. Zaman, Z. Zhou, L. Cao, X.-Q. Gong and J. Yang, *Chem. Commun.*, 2018, **54**, 996–999.
25 L. Fang, W. X. Li, Y. Guan, Y. Feng, H. Zhang, S. Wang and Y. Wang, *Adv. Funct. Mater.*, 2017, **27**(24), 1701008.
26 D. G. Wang, X. W. Zhang, G. C. Guo, S. H. Gao, X. X. Li and J. H. Meng, *et al.*, Large-Area Synthesis of Layered $HfS_{2(1-x)}Se_{2x}$ Alloys with Fully Tunable Chemical Compositions and Bandgaps, *Adv. Mater.*, 2018, **30**(44), 1803285.
27 K. Selvakumar, S. M. Senthil Kumar, R. Thangamuthu, G. Kruthika and P. Murugan, *Int. J. Hydrogen Energy*, 2014, **39**(36), 21024–21036.
28 C. Chen, Y. J. Kang, Z. Y. Huo, Z. W. Zhu, W. Y. Huang and H. L. Xin, *Science*, 2014, **343**(6177), 1339–1343.
29 Z. J. Zhao and J. L. Gong, *Nat. Nanotechnol.*, 2022, **17**, 563–564.
30 K. Xu, X. Lin, X. Wang, L. Li, Z. Zhu and Y. Tian, *Appl. Surf. Sci.*, 2018, **459**, 782–787.
31 R. U. Chandrasena, O. Yang, Q. Lei, M. U. Delgado-Jaime, K. D. Wijesekara and M. Golalikhani, *Nano Lett.*, 2017, **17**(2), 794–799.
32 Z. M. Chan, D. A. Kitchaev, J. N. Weker, C. Schnedermann, K. Lim, G. Ceder, W. Tumas, M. F. Toney and D. G. Nocera, *Proc. Natl. Acad. Sci. U. S. A.*, 2018, **115**(23), e5263–e5268.
33 J. Liu, T. Wang, M. Sun, M. Liao, S. Wang, S. Liu, H. Shi, Y. Liu, Y. Shen, R. Cao, Y. Huang, B. Huang and Q. Li, *J. Am. Chem. Soc.*, 2024, **146**(48), 33276–33287.
34 J. Zhu, F. Liu, G. B. Stringfellow and S.-H. Wei, *Phys. Rev. Lett.*, 2010, **105**, 195503.
35 P. G. Harrison, N. C. Lloyd and W. Daniell, *J. Phys. Chem. B*, 1998, **102**(52), 10672–10679.
36 P. F. Liu, S. Yang, L. R. Zheng, B. Zhang and H. G. Yang, *Chem. Sci.*, 2017, **8**, 3484–3488.
37 S. Yagi, I. Yamada, H. Tsukasaki, A. Seno, M. Murakami, H. Fujii, H. Chen, N. Umezawa, H. Abe, N. Nishiyama and S. Mori, *Nat. Commun.*, 2015, **6**, 8249.
38 K. Ham, S. Kang, Y. Kim, Y. Lee, Y.-D. Kim and J. Lee, Participation of the Unstable Lattice Oxygen of Cation-Exchanged δ-MnO_2 in the Water Oxidation Reaction, *J. Mater. Chem. A*, 2023, **11**, 21686–21693.
39 X. Li, J. Wang, H. Xue, L. Zhao, J. Lu and H. Zhang, *Adv. Funct. Mater.*, 2025, 2503360.
40 Z. Wang, R. Lin, Y. Huo, H. Li and L. Wang, *Adv. Funct. Mater.*, 2022, **32**, 2109503.
41 N. Zhang, X. Feng, D. Rao, X. Deng, L. Cai and B. Qiu, *Nat. Commun.*, 2020, **11**, 4066.
42 K. Zhu, F. Shi, X. Zhu and W. Yang, *Nano Energy*, 2020, **73**, 104761.
43 L. Yao, Z. Geng, W. Zhang, X. Wu, J. Liu and L. Li, *ACS Sustainable Chem. Eng.*, 2020, **8**(46), 17194–17200.
44 T. Subramaniam, B. S. Krishnaveni and S. Devaraj, *J. Mater. Sci.: Mater. Electron.*, 2024, **35**, 1184.
45 Q. Zhuang, N. Ma, Z. Yin, X. Yang, Z. Yin, J. Gao, Y. Xu, Z. Gao, H. Wang, J. Kang, D. Xiao, J. Li, X. Li and D. Ma, *Adv. Energy Sustainability Res.*, 2021, **2**(8), 2100030.
46 C. Wei, C. Li, J. Liu, H. Huang and S. Wu, *Catal. Lett.*, 2024, **154**, 3541–3551.
47 Q. Ma and S. Mu, *Interdiscip. Mater.*, 2023, **2**, 53–90.
48 Q. Hu, X. Liu, C. Tang, L. Fan, X. Chai, Q. Zhan, J. Liu and C. He, *Electrochim. Acta*, 2018, **265**, 620–628.
49 L. Zeng, T. S. Zhao, R. H. Zhang and J. B. Xu, *Electrochem. Commun.*, 2018, **87**, 66–70.
50 Y. Xiong, L. Xu, C. Jin and Q. Sun, *Appl. Catal., B*, 2019, **254**, 329–338.
51 X. Xiong, Y. Ji, M. Xie, C. You, L. Yang, Z. Liu, A. M. Asiri and X. Sun, *Electrochem. Commun.*, 2018, **86**, 161–165.
52 H. Liao, X. Guo, Y. Hou, H. Liang, Z. Zhou and H. Yang, *Small*, 2020, **16**(10), 1905223.
53 G. Liu, J. Pan, L. Yin, J. T. Irvine, F. Li and J. Tan, Heteroatom-Modulated Switching of Photocatalytic Hydrogen and Oxygen Evolution Preferences of Anatase TiO_2 Microspheres, *Adv. Funct. Mater.*, 2012, **22**, 3233–3238.
54 M. G. Ahmed, Y. F. Tay, X. Chi, A. S. Razeen, Y. Fang, M. Zhang, A. Sng, S. Y. Chiam, A. Rusydi and L. H. Wong, *Angew. Chem., Int. Ed.*, 2025, **64**(9), e202416757.
55 W. Ou, S. D. Marks, R. F. de Menezes, R. He, Z. Zhang, C. Sindt, J. Thurston, C. Jaye, B. Cowie, L. Thomsen, Z. Zhuo, J. Guo, W. Yang, Z. Dong, R. Tenent, K. G. Sprenger and Ml. F. Toney, *Adv. Energy Mater.*, 2025, 2404652.
56 J. Polonsky, P. Mazur, M. Paidar, E. Christensen and K. Bouzek, *Int. J. Hydrogen Energy*, 2014, **39**(7), 3072–3078.
57 J. Kenneth Klewicki and James J. Morgan, *Environ. Sci. Technol.*, 1998, **32**(19), 2916–2922.
58 C. Walter, S. Kalra, R. Beltrán-Suito, M. Schwarze, P. W. Menezes and M. Driess, *Mater. Today Chem.*, 2022, **24**, 100905.
59 H. Ooka, T. Takashima, A. Yamaguchi, T. Hayashiab and R. Nakamura, *Chem. Commun.*, 2017, **53**, 7149–7161.
60 T. Takashima, K. Hashimoto and R. Nakamura, *J. Am. Chem. Soc.*, 2012, **134**(3), 1519–1527.
61 S. Panimalar, S. Logambal, R. Thambidurai, C. Inmozhi, R. Uthrakumar and A. Muthukumaran, *Environ. Res.*, 2022, **205**, 112560.
62 S. P. Babu and A. Falch, *ChemCatChem*, 2022, **14**(15), e202200364.
63 C. Rong, X. Huang, H. Arandiyan, Z. Shao, Y. Wang and Y. Chen, *Adv. Mater.*, 2025, **37**(9), 2416362.
64 T. Reier, Z. Pawolek, S. Cherevko, M. Bruns, T. Jones, D. Teschner, S. Selve, A. Bergmann, H. N. Nong, R. Schlögl, K. J. J. Mayrhofer and P. Strasser, *J. Am. Chem. Soc.*, 2015, **137**(40), 13031–13040.
65 W. Jia, X. Cao, X. Chen, H. Qin, L. Miao and Q. Wang, *Small*, 2024, **20**(34), 2310464.
66 C. Hu, K. Yue, J. Ha, X. Liu, L. Liu, Q. Liu, Q. Kong, C.-W. Pao, Z. Hu, K. Suenaga, D. Su, Q. Zhang, X. Wang, Y. Tan and X. Huang, *Sci. Adv.*, 2023, **9**(37), eadf9144.
67 Z. Shi, Y. Wang, J. Li, X. Wang, Y. Wang, Y. Li, W. Xu, Z. Jiang, C. Li, W. Xing and J. Ge, *Joule*, 2021, **5**, 2164–2176.
68 X. Chen, R. Ma, W. Jia, X. Cao, J. Zhang, F. Cheng and L. Jiao, *Chem. Catal.*, 2025, **5**, 101335.

69 J. F. de Araújo, F. Dionigi, T. Merzdorf, H.-S. Oh and P. Strasser, *Angew. Chem., Int. Ed.*, 2021, **60**(27), 14981–14988.
70 H. Li, W. Wang, S. Xue, J. He, C. Liu, G. Gao, S. Di, S. Wang, J. Wang, Z. Yu and L. Li, *J. Am. Chem. Soc.*, 2024, **146**(13), 9124–9133.
71 K. A. Stoerzinger, W. S. Choi, H. Jeen, H. N. Lee and Y. Shao-Horn, *J. Phys. Chem. Lett.*, 2015, **6**, 487.
72 D. Pesquera, G. Herranz, A. Barla, E. Pellegrin, F. Bondino, E. Magnano, F. Sanchez and J. Fontcuberta, *Nat. Commun.*, 2012, **3**, 1189.
73 Q. Yan, Y. Li, Y. Wu, Y. Li, C. Yang, L. Ban, Y. Zhao, B. Dai, G. Wan, Y. Li, J. Zhang, Z. Wang, H. Pang and F. Yu, *EES Catal.*, 2025, **3**, 407–419.
74 X. Ping, Y. Liu, L. Zheng, Y. Song, L. Guo, S. Chen and Z. Wei, *Nat. Commun.*, 2024, **15**, 2501.